*Journal of Structural Geology*, Vol. 11, No. 8, pp. 959 to 974, 1989
Printed in Great Britain

0191-8141/89 $03.00+0.00


# Fault-fracture strain in Wingate Sandstone

WILLIAM R. JAMISON

Amoco Production Research, P.O. Box 3385, Tulsa, OK 74102, U.S.A.

(*Received* 5 *April* 1988; *accepted in revised form* 5 *April* 1989)

**Abstract**—The Laramide deformation of the Triassic Wingate Sandstone along the northeast flank of the Uncompahgre uplift has occurred by faulting at various scales. Macroscopically smooth flexures of beds within the Wingate occur by small displacements across a myriad of intraformational, mesoscale faults. The deformation resultant from these small faults may be approximated by a strain tensor, provided the measurement domain satisfies certain size criteria. Equivalent strain ($\bar{\varepsilon}$) measurements, obtained from 22 locations in the East Kodel's Canyon, range from 1% to 15.5% (the maximum contractional strains range from −0.9% to −13.4%). The faults producing this strain have displacements ranging from a fraction of a millimeter to 18.5 cm.

The fault intensity increases with increasing $\bar{\varepsilon}$, although in a distinctly non-linear fashion. At low strains, incremental increases in the deformation produce additional, small displacement faults. At larger strains, incremental increases in the deformation occur via progressive displacement along existing faults. The principal strain axes are consistently non-coaxial with the inferred principal stresses (average $\sigma_1 \wedge \varepsilon_1$ is 18.5°). This non-coaxiality results from the non-uniform development of the conjugate fault systems. This same inequality of the conjugate systems produces a non-zero rotation tensor, $\omega$, but $\omega$ is not related to $\sigma_1 \wedge \varepsilon_1$. The non-uniform development of conjugate shears (and the associated non-coaxiality of $\sigma_1$ and $\varepsilon_1$) may be an intrinsic characteristic of a Coulomb material.

## INTRODUCTION

EAST Kodel's Canyon is one of several canyons where forced folded and faulted Triassic Wingate Sandstone is exposed along the northeast flank of the Uncompahgre Plateau (Fig. 1) in Colorado and Utah (Lohman 1965). The structure in the sedimentary rocks in East Kodel's Canyon (Fig. 2) developed in response to Laramide dip-slip displacement on high-angle faults in the underlying basement. Deformation within the Wingate occurred almost exclusively by faulting at various scales (Jamison & Stearns 1982). One major fault zone cuts entirely through the 100 m thick Wingate Formation at East Kodel's Canyon, but most of the faults have an outcrop length of a few meters or less and displacements of a fraction of a millimeter to a few centimeters. Beds within the Wingate Formation display drag flexure within 40 m of the major fault zone. These flexures, which are quite smooth at the macrosopic scale, occur by small, discrete displacements across myriads of the small, intraformational faults (Jamison & Stearns 1982).

Small faults, like those in the Wingate Sandstone (Fig. 3), are very common deformational features in most rocks that have been deformed in their 'brittle' regime. These small faults, also known as shear fractures (especially where displacements are not obvious), can contribute significantly to the overall deformation of a rock. The deformation produced by these shear features is additive to the effects of other strain-producing mechanisms (e.g. pressure solution, twin gliding) that may also have been active.

Several procedures for inferring principal strain ratios from fault orientations and slip directions have been published (e.g. Arthaud 1969, Reches 1978, Krantz 1988), but little progress has been made in actually quantifying the strain resulting from displacement along faults and fractures. The reason for this is two-fold. First, faults and fractures produce deformation via displacements across discrete surfaces. Thus, the deformation is discontinuous. Strain, on the other hand, is strictly a continuum measurement. However, the distinction between continuous and discontinuous is a matter of scale. Recently, Gauthier & Angelier (1985) have presented a technique for fault-strain determination for the case where the rock mass being studied is large relative to displacements on the individual faults. The second impediment to fault-strain calculations is a practical limitation. Quantitative assessment of fault strain requires a determination of sense and magnitude of displacement on *all* faults in the rock mass being studied. Adequate markers to allow these measurements are seldom available and accessible.

The Wingate Sandstone has well-defined cross-bed surfaces, providing abundant markers for assessing fault displacements. In East Kodel's Canyon the small faults consistently are strike-parallel to the main fault and have dip-slip slickenside lineations. Also, large, clean and accessible outcrops of the Wingate are common. The practical limitations to obtaining the requisite measurements for fault-strain determinations are, consequently, largely eliminated in the East Kodel's Canyon structure.

Expressing the fault-related deformation in terms of strain provides a quantitative appreciation of the role of mesoscale faulting in the development of the Wingate structures. Making full use of all the deformational data that can be obtained from these small faults also provides some insight into the deformational behavior of a general Coulomb material. First, though, conversion of outcrop measurements into meaningful strain values requires not only the concept of a fault-strain tensor, but

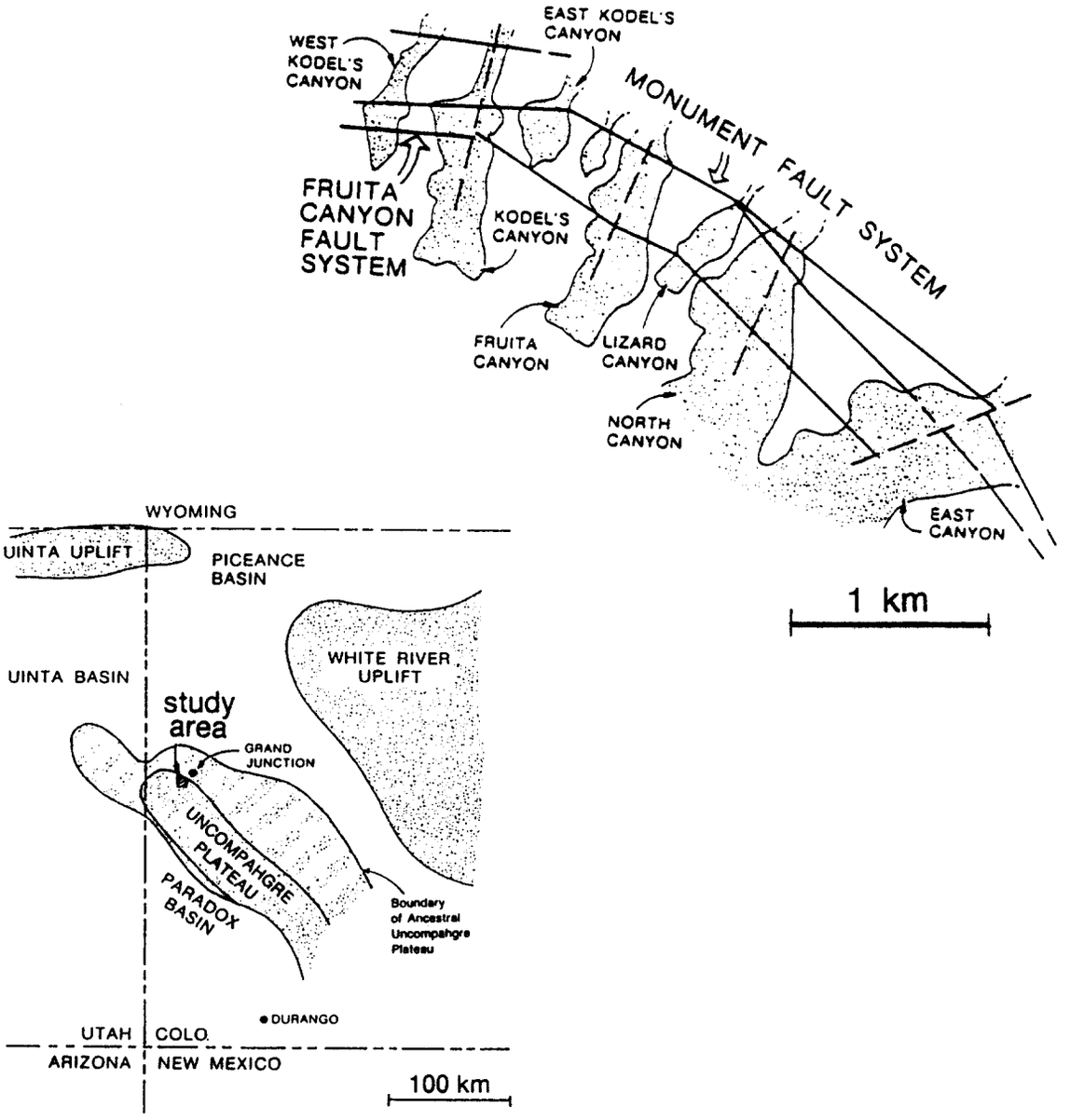


Fig. 1. Location map of East Kodel's Canyon and adjacent canyons along the northeast flank of the Uncompahgre Plateau. The Monument and Fruit Canyon fault systems consist of high-angle faults in the crystalline basement that induced forced folds and faults in the overlying sedimentary rocks. These faults consistently downdrop to the N or NE.

also considerations of an appropriate sampling domain size.

## FAULT STRAIN

### *The fault-strain tensor*

If the area being examined is large relative to both the spacing and offsets on the included faults, it is easy to accept that the resultant deformation is approximately represented by a smooth strain ellipse (Fig. 4). This ellipse, and the strain tensor, is the sum of the effects of the individual faults. The fault-strain determination thus begins with a consideration of the effect of individual features.

Following the procedure of Gauthier & Angelier (1985), the deformation is initially expressed in terms of the displacement gradient tensor, $D_{ij}$.

Presently restricting the discussion to the two-dimensional (plane strain) situation:

$$D_{ij} = \begin{bmatrix} \partial u/\partial x & \partial u/\partial y \\ \partial v/\partial x & \partial v/\partial y \end{bmatrix}. \quad (1)$$

For a circle of diameter $d$, cut by a fault of displacement $s$ parallel to the $y$-axis (Fig. 5a), this displacement-gradient tensor is approximated by

$$D_{ij} = \begin{bmatrix} 0 & 0 \\ s/d & 0 \end{bmatrix}. \quad (2)$$

This approximation is tantamount to distributing the fault displacement uniformly along the $x$-axis across the circle. In this illustration, the fault is in the center of the

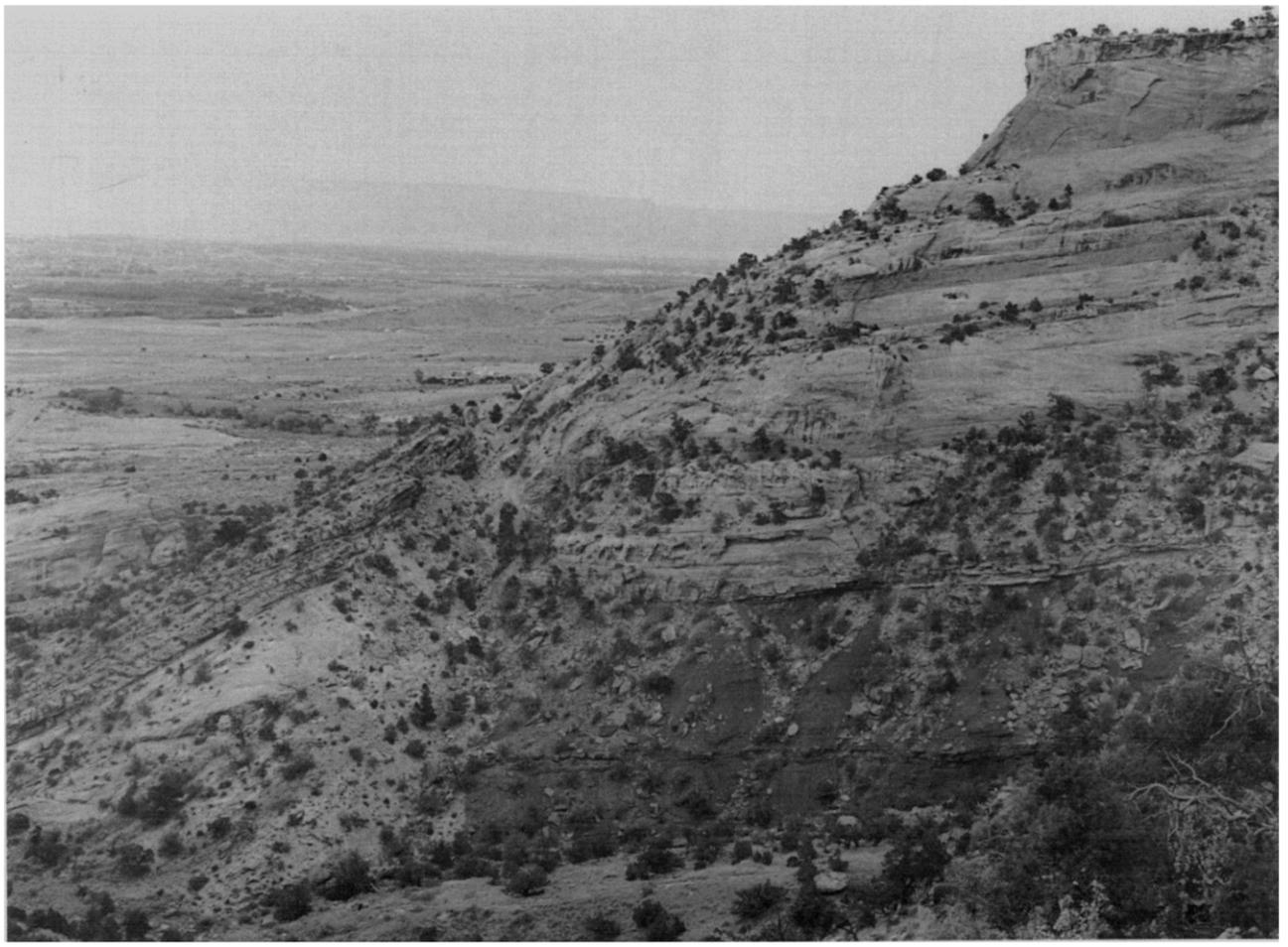

Fig. 2. Outcrop of the Triassic Wingate Sandstone on the east wall of East Kodel's Canyon. The cliff faces of Wingate Sandstone are capped by the more resistant, basal beds of the Triassic Kayenta Sandstone. The Wingate is underlain by the Triassic Chinle Formation, a redbed sequence.

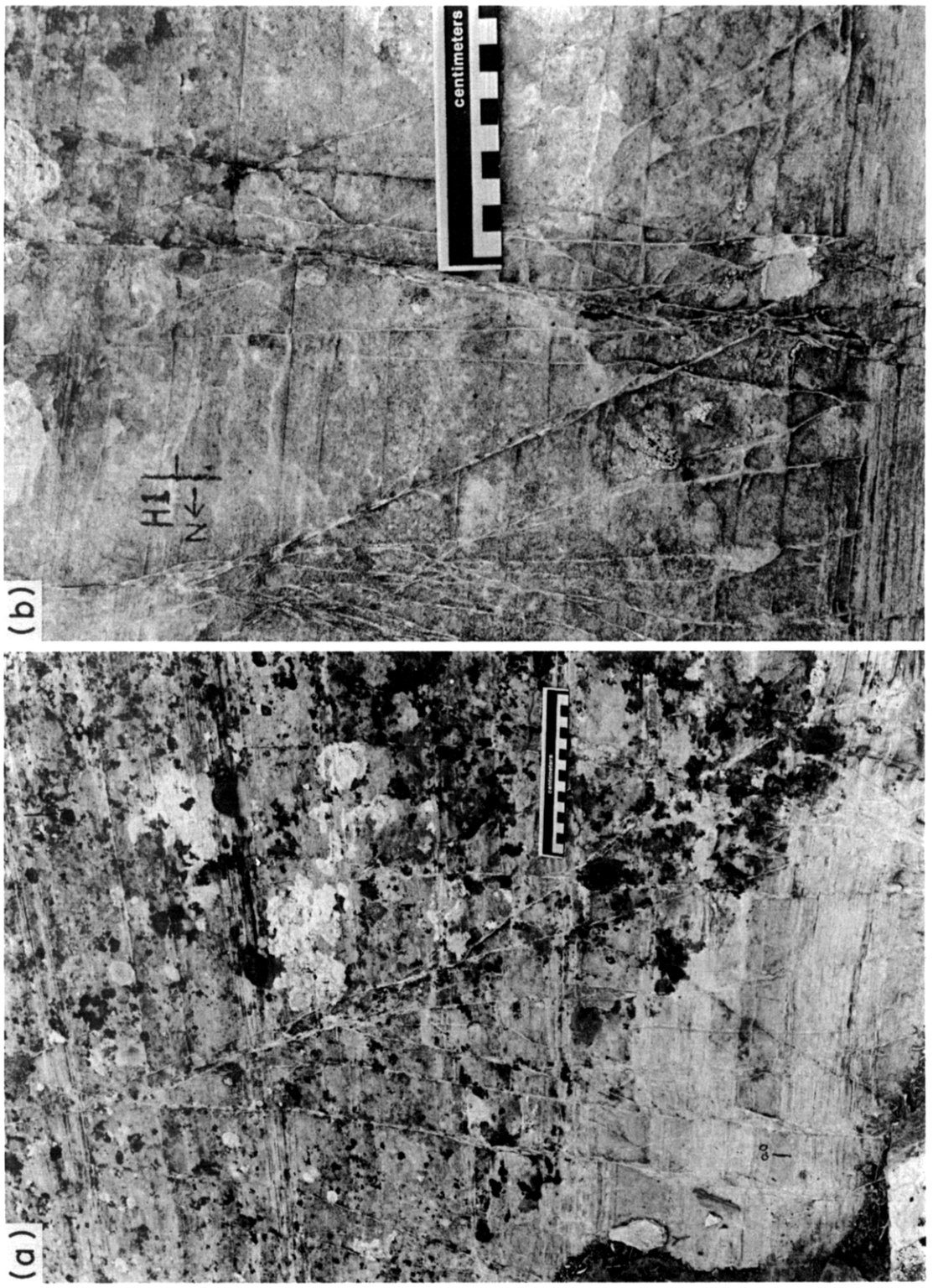


Fig. 3. Mesoscale, intraformational faults in the Wingate Sandstone.

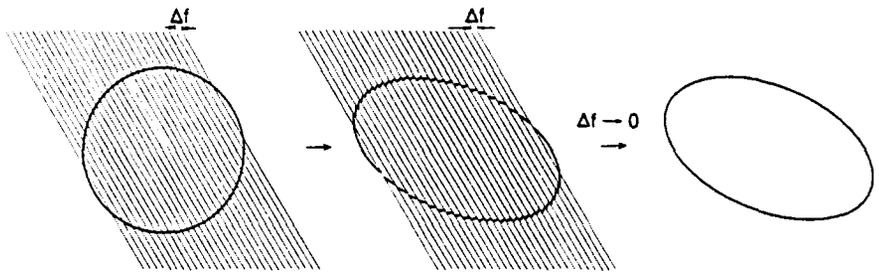


Fig. 4. Small fault displacements will convert a circle into a 'broken ellipse'. If the spacing between the faults (Δf) becomes very small, this 'broken ellipse' approximates a smooth 'strain ellipse'.

circle, but the same formulation is appropriate regardless of where the fault lies within the circle. Rotation to a reference co-ordinate system (Fig. 5b) is by standard tensor transformation (e.g. Nye 1972)

$$D_{mn} = a_{mi}a_{nj}D_{ij}, \tag{3}$$

where

$$a_{kl} = \begin{bmatrix} \sin\theta & -\cos\theta \\ \cos\theta & \sin\theta \end{bmatrix}, \tag{4}$$

so,

$$D_{mn} = \frac{s}{d}\begin{bmatrix} -\sin\theta\cos\theta & -\cos^2\theta \\ \sin^2\theta & \sin\theta\cos\theta \end{bmatrix}. \tag{5}$$

If the circle is intersected by several faults, the values of $s$ and $\theta$ used to calculate the individual displacement-gradient tensors will, in general, be different for each fault. However, $d$ defines the size of the area being considered, and does not vary. To assess the deformation due to all of the faults intersecting the circle (the sample domain), the displacement-gradient tensors of all the individual faults (expressed in terms of a common reference co-ordinate system) are simply summed to give the composite displacement-gradient tensor $D^c_{mn}$. For small deformations, $D^c_{mn}$ may be decomposed into its symmetric and skew-symmetric parts to give the strain ($\varepsilon$) and rotation ($\omega$) tensors, respectively:

$$D^c_{mn} = \varepsilon_{mn} + \omega_{mn}. \tag{6}$$

For larger deformations, the expressions for strain involve higher order terms (e.g. Fung 1965). All of these are found in the displacement-gradient tensor (see Appendix).

The eigenvectors and eigenvalues of the strain tensor, $\varepsilon_{mn}$, are the principal strain axes and the principal strain magnitudes, respectively. Strain magnitudes may also be expressed as equivalent uniaxial strain, $\bar{\varepsilon}$, a scalar value:

$$\bar{\varepsilon} = [\tfrac{2}{3}(\varepsilon_{ij}\cdot\varepsilon_{ij})]^{1/2} = (\tfrac{2}{3}I_2)^{1/2}, \tag{7}$$

where $\varepsilon_{ij}$ are the components of the strain tensor and $I_2$ is the second invariant of strain (Bisplinghoff *et al.* 1965, Jaeger & Cook 1969). For volume constant deformation $\bar{\varepsilon}$ is slightly larger in magnitude than either the maximum contraction or extension (e.g. see Table 1). Expressed in terms of the principal strain axes ($\varepsilon_1$, $\varepsilon_2$, and $\varepsilon_3$):

$$\bar{\varepsilon} = [\tfrac{2}{9}((\varepsilon_1-\varepsilon_3)^2 + (\varepsilon_2-\varepsilon_3)^2 + (\varepsilon_1-\varepsilon_2)^2)]^{1/2}. \tag{8}$$

Note that by simply modifying the displacement-gradient tensor for the individual deformational feature, this strain determination procedure may be extended to other 'discontinuous' deformational features, such as extension fractures (joints) and stylolites (see Appendix). For three-dimensional strain analyses, the procedure is parallel to that outlined above (see Appendix).

*Sampling domain size*

The choice of $d$, the sample domain diameter, is a factor of critical importance in the fault-strain determination. Too small a sample domain is undesirable because the discontinuous aspect of the deformation remains pronounced. A small change in the sample domain size may result in a very large change in the calculated strain. If a very large sample domain is used, significant variations in the deformation may be lumped into a single strain measurement. Strain determinations through a geological structure are commonly undertaken specifically to quantify these variations. Thus, it is counterproductive to choose too large an area for a

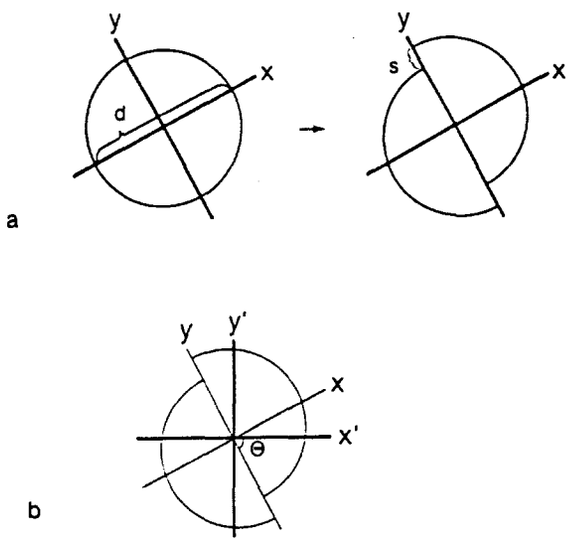


Fig. 5. Determination of the displacement-gradient tensor, in two dimensions, for faulting. (a) Displacement '$s$' along a fault parallel to the $y$-axis. (b) Rotation to a reference co-ordinate system, $x'y'$, may be expressed in terms of $\theta$, the dip of the fault in the $x'y'$ system.

Table 1. Description of fault populations at measurement stations in East Kodel's Canyon (see Fig. 8 for station locations), and calculated fault strains

| Station | Domain diameter (m) | No. of faults | Largest fault offset (cm) | No. of large faults | No. of medium faults | Quality rating* | $\bar{\varepsilon}$ (%) | $\varepsilon_1$ (%) |
|---|---|---|---|---|---|---|---|---|
| A | 1.0 | 19 | 3.8 | 2 | 1 | M | 1.21 | −1.05 |
| B | 1.0 | 19 | 2.7 | 5 | 0 | A | 1.96 | −1.70 |
| C | 1.5 | 58 | 1.9 | 5 | 5 | A | 1.45 | −1.41 |
| D | 1.0 | 18 | 13.7 | 3 | 4 | A | 0.98 | −0.90 |
| E | 1.0 | 27 | 2.2 | 1 | 3 | M | 1.13 | −1.08 |
| F | 0.65 | 42 | 1.9 | 2 | 5 | M | 6.07 | −5.46 |
| G | 1.0 | 19 | 2.2 | 2 | 2 | M | 3.00 | −2.60 |
| H | 0.75 | 43 | 11.7 | 2 | 3 | M | 15.45 | −13.54 |
| I | 1.1 | 50 | 11.7 | 2 | 2 | M | 8.71 | −7.69 |
| J | 1.0 | 37 | 4.3 | 6 | 2 | A | 9.67 | −8.34 |
| K | 1.0 | 42 | 10.0 | 1 | 2 | M | 11.02 | −9.70 |
| L | 1.0 | 51 | 9.5 | 2 | 1 | M | 9.25 | −8.13 |
| M | 0.5 | 27 | 5.7 | 1 | 1 | S | 5.70 | −5.03 |
| N | 0.5 | 31 | 0.6 | 3 | 5 | A | 1.65 | −1.57 |
| O | 1.0 | 12 | 2.2 | 4 | 4 | A | 3.11 | −2.69 |
| P | 1.0 | 10 | 1.9 | 2 | 1 | M | 1.57 | −1.38 |
| Q | 1.0 | 48 | 1.9 | 3 | 2 | A | 3.05 | −2.75 |
| R | 1.5 | 30 | 6.2 | 6 | 2 | A | 9.48 | −8.18 |
| S | 1.0 | 54 | 3.2 | 4 | 4 | A | 6.15 | −5.49 |
| T | 1.0 | 40 | 4.9 | 5 | 1 | A | 10.68 | −9.34 |
| U | 1.0 | 37 | 18.3 | 1 | 1 | S | 12.17 | −10.46 |
| V | 0.33 | 31 | 5.0 | 1 | 1 | S | 9.99 | −8.86 |

*A—highly appropriate; M—marginally suitable; S—suspect. See section on 'Fault strain in the Wingate'.

single determination of fault strain. The sampling domain should be small enough that the deformation is reasonably homogeneous throughout the domain, yet large enough to avoid significant changes in the calculated strain by minor changes in the domain size.

Empirical tests with a few simple, hypothetical fault populations (see Appendix) suggest that a reasonably consistent strain determination should result if the largest three or four faults in the sample have similar displacement magnitudes. The effect of sampling domain size may also be illustrated with one of the data sets (station I) from the East Kodel's Canyon structure. A total of 50 mesoscale faults occur within a sampling domain that is 1.1 m in diameter. Most of these faults have very small offsets. Only six faults have displacements greater than 1.0 cm, the largest having an offset of 11.7 cm. All detectable slickensides in the area lie within a common plane. Therefore, plane strain (using the plane of the slickensides) is assumed for the fault-strain calculations.

A total of 22 independent fault-strain values are derived from this data set by using sampling domains with diameters ($d$) ranging from 5 cm to 1.1 m, in 5 cm increments (Fig. 6). Each strain value is calculated using all faults within the given domain. There are major variations in the calculated $\bar{\varepsilon}$ for the smaller diameter domains, and there is also a significant change in $\bar{\varepsilon}$ each time the domain size is increased just enough to include another of the large-displacement faults. The minimum acceptable domain size is a subjective judgement. The hypothetical cases (Appendix) suggest that a useful sampling domain should, at a minimum, include three of the large-offset faults, and the boundaries of the domain should not be too close to any of these faults. This would suggest a domain diameter of about 90 cm is adequate for this particular sample location. For $d$ = 90 cm, $\bar{\varepsilon}$ is about 10%. Increasing the diameter of the sampling domain probably does not, in fact, 'improve' the calculated $\bar{\varepsilon}$.

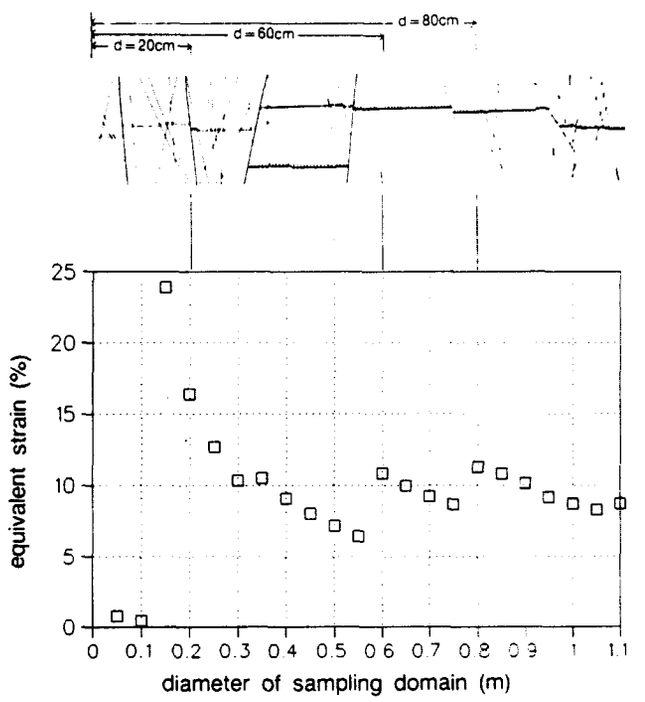


Fig. 6. Fault development at Station I. (a) Fault orientations and displacements in the plane of the strain calculation. (b) Calculated $\bar{\varepsilon}$ for various sample domain diameters.

## THE EAST KODEL'S CANYON STRUCTURE

The East Kodel's Canyon structure is dominated by a vertical fault that offsets the top of the Wingate Formation approximately 45 m (Figs. 2 and 7). Much of the Wingate section is well exposed and accessible in the upthrown block. Mesoscale faults occur throughout most of the upthrown Wingate to a distance of 100–150 m from the main fault. In the upper third of the Wingate Formation the distribution of these small faults is much more restricted. (Relative to the numerous other exposures through similar Wingate structures along this flank of the Uncompahgre, the width of the deformation zone here is quite broad. More commonly, mesoscale faults in the upthrown block occur only to a distance of a few tens of meters from the main fault.) In the downthrown block at East Kodel's Canyon, only the upper 20–30 m of the 100 m thick Wingate Formation is exposed. Mesoscale faults occur through this exposed portion of the downthrown block to a distance of 75–90 m from the main fault.

The outcrop lengths of the mesoscale faults are several tens of centimeters to several meters. These faults are all intraformational to the Wingate, and most are restricted to individual bedding units, which are generally a few meters thick. Shear displacements on most of these faults are less than a few millimeters, but some have several centimeters or tens of centimeters offset. In the East Kodel's Canyon outcrops, the largest observed fault offsets, excepting the main fault, are about 25 cm.

Earlier efforts to quantify the deformation in the Wingate (Jamison & Stearns 1982) include the measurement of both the density and the intensity (Fig. 7) of the small fault development through the East Kodel's Canyon structure. Measurement traverses are parallel to bedding and roughly perpendicular to the faults. Density is the number of faults per meter. The very small displacement faults are clearly defined by a single, discrete gouge zone along the fault surface (see Fig. 3). At increasing displacements, additional gouge zone segments form along the fault in an anastomosing configuration (Aydin & Johnson 1978, Jamison & Stearns 1982). I have estimated the average number of gouge zones associated with each fault, and define the fault intensity as the number of gouge zones per meter. Since each fault has one or more gouge zones, fault intensity must be equal to or greater than fault density.

In general, fault intensity increases toward the main fault and decreases upsection (Fig. 7), though there are obvious departures from this generalization. In the downthrown block, a relatively high intensity zone occurs along a conspicuous flexure, perhaps a precursor to another through-going fault. The relatively high fault intensity zone in the upthrown block, about 80 m from the main fault, has no clear genetic association.

### *Fault strain in the Wingate*

Throughout the East Kodel's Canyon outcrops, slickensides on the mesoscale faults consistently indicate dip-slip movement, and the strikes of these small faults are usually no more than ±20° from the strike of the main fault. Thus, motion along the faults occurs primarily in the plane of the cross section (the plane perpendicular to the main fault). Consequently, the strain calculations have been simplified to a two-dimensional assessment (plane strain in the plane of the cross-section, oriented N20E/vertical).

Although fault-strain determinations are possible at many locations throughout the East Kodel's Canyon structure, I have focused my assessments in the areas that provoke a minimum of measurement error and reflect a simple deformational history. The sampling stations for the strain determinations are restricted,

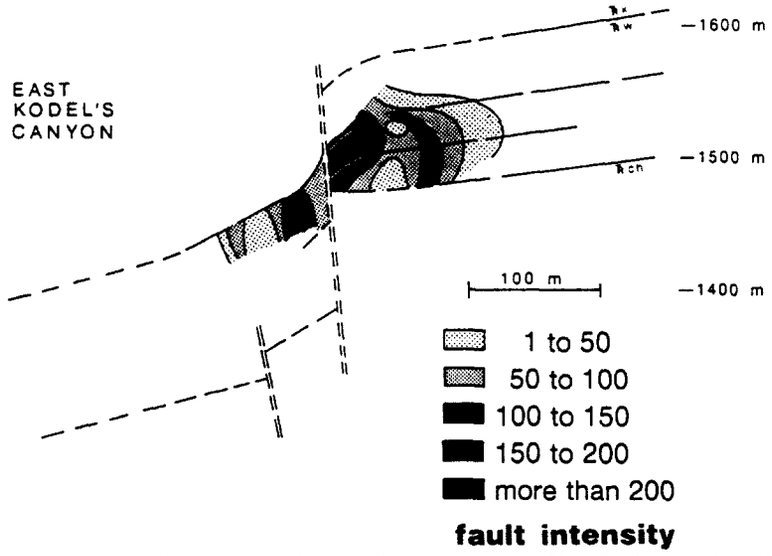


Fig. 7. Fault intensities throughout the deformed Wingate Sandstone in East Kodel's Canyon (from Jamison & Stearns 1982). Map is on surveyed outcrop projected into the plane of the cross-section (N20E/90).

primarily, to one particular bed, 60–65 m above the base of the formation in the upthrown block (Fig. 8). All sampling locations are on steep outcrop surfaces that are close, in attitude, to the cross-section plane. Sampling domain sizes range from 0.33 to 1.5 m in diameter, with the majority being 1 m across (Table 1).

The outcrop data were collected before the effects of sampling domain size were fully appreciated, so the chosen sizes were more a function of convenience than forethought. In order to provide some estimate of the appropriateness of the collected sample populations for strain determination, as per the empirical guidelines discussed above, the individual populations are assigned a rating based on the number of large-displacement faults. 'Large' is both subjective and relative. For this rating, a large fault is defined as any fault that has a displacement that is at least 40% of the displacement on the largest-offset fault in the sampling domain. A medium fault is one with an offset between 20% and 40% of the displacement of the largest-offset fault. A sampling population with at least three large faults is considered highly appropriate (A) for a fault strain determination. One with less than three large faults, but at least three medium to large faults, is deemed marginally suitable (M) for a strain representation. If there are only one or two medium or large faults, the calculated strain magnitudes are suspect (S). Of the 22 data sets collected, 10 are rated A, nine are rated M and three fall into the S category (Table 1).

*Fault strain and fault density/intensity*

The equivalent strains ($\bar{\varepsilon}$) produced by mesoscale faults in the Wingate, as measured at the 22 sampling stations, range from 0.98% to 15.45% (Table 1). This variation in the strain magnitudes reflects differences in the cumulative fault displacement, which, in turn, depends on the number of faults and the displacement on the individual faults. These latter two parameters also determine fault density and intensity. Consequently, it might be expected that fault strain is functionally related to fault intensity and/or density. To assess this relationship, strain magnitude is plotted against both density and intensity (Fig. 9). Piecewise-linear regression segments are fitted to these data, assuming strain to be the independent variable. The linear segment between 0 and 0.95% $\bar{\varepsilon}$ on both plots is unconstrained by data. It simply connects the second linear segment to the origin.

The linear fits to the data suggest that both density and intensity increase with increasing fault strain up to about 3.5% $\bar{\varepsilon}$. At larger strains, the intensity continues to increase as the strain increases, though at a noticeably reduced rate. Fault density, however, shows no consistent increase above 3.5% $\bar{\varepsilon}$. One interpretation for these relationships may be that, at the smaller strains, each incremental increase in strain occurs via the development of additional, very small displacement faults. This produces similar increases in both fault intensity and density. At the larger strains, however, incremental increases in fault strain result primarily from progressive displacement on existing faults, with little or no additional fault generation. As noted above, increased offset on these faults usually results in the creation of additional gouge zone segments, thus producing an increase in fault intensity while fault density is relatively unchanged.

This interpretation is commensurate with general field observations made as the data were collected, viz., that the large-strain populations have just a few relatively large-offset faults. At most sampling locations, these few large faults account for most of the calculated

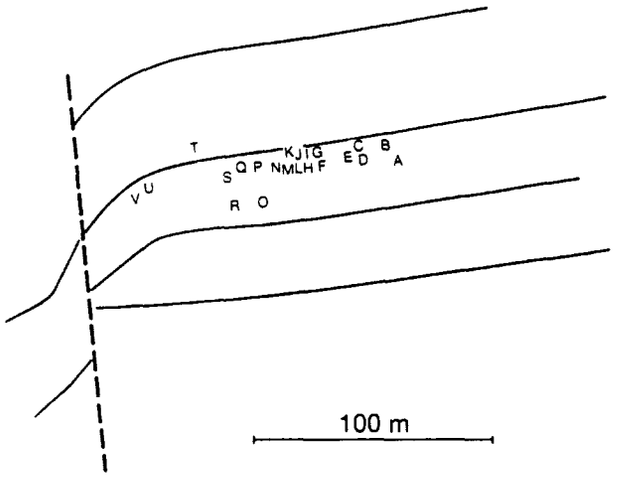


Fig. 8. Location map of strain measurement stations on the East Kodel's Canyon structure (cf. Figs. 2 and 7).

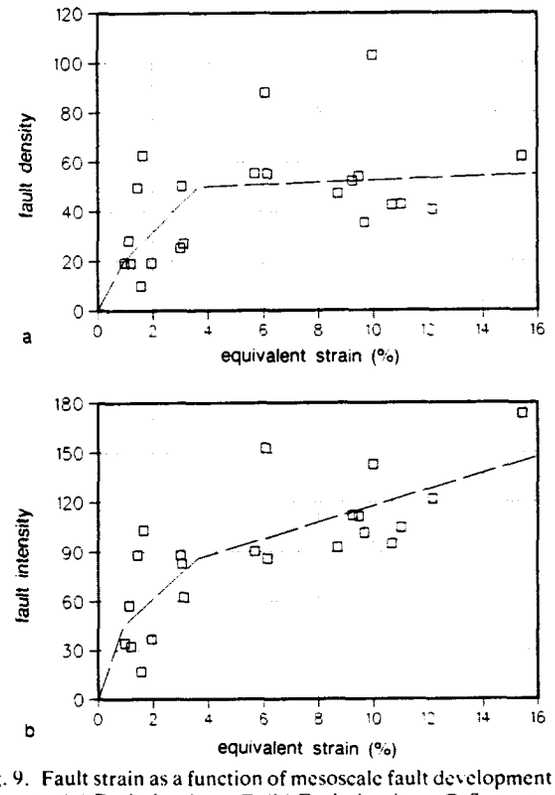


Fig. 9. Fault strain as a function of mesoscale fault development in the Wingate. (a) Fault density vs $\bar{\varepsilon}$. (b) Fault density vs $\bar{\varepsilon}$. Separate linear fits for the data from 0.95 to 3.5% $\bar{\varepsilon}$ and 3.5% to 15.5% $\bar{\varepsilon}$.

strain. For example, at station I (see Table 1), there are 50 faults, but only six have displacements greater than 1.0 cm (the largest offset being 11.7 cm). These six large-displacement faults account for 80% of the 8.7% $\bar{\varepsilon}$ at this location. Pursuing the interpretation of fault development mentioned above, the deformation at station Q could be viewed as an earlier stage of the station I deformation. The fault densities at stations Q and I are almost identical. At station Q, which has 3.05% $\bar{\varepsilon}$, the largest fault offset is 1.9 cm and there are only two faults with displacements greater than 1.0 cm. The evolution from Q to I (from 3.05% to 8.7% $\bar{\varepsilon}$) could have occurred via progressive offset on five or six of the existing faults.

While this model may have general validity, there are clear exceptions to the rule. At station F, over 6% $\bar{\varepsilon}$ occurs via a multitude (fault density = 88) of relatively small displacement faults (only one fault with over 1.0 cm offset). In contrast, less than 2% $\bar{\varepsilon}$ occurs at station B (fault density = 19), yet there are five faults with over 1.0 cm displacement. The specific history of fault development and offset is obviously quite variable.

The suggested piecewise-linear relationship between fault strain and fault intensity may be used, cautiously, to convert the measured fault intensities in the Wingate into approximate strain values (Fig. 10). This conversion indicates that, throughout most of the East Kodel's Canyon structure, the strains resulting from the mesoscale faults are less than a few percent $\bar{\varepsilon}$. In the high fault intensity zone adjacent to the main fault, on the upthrown block, the fault strains may exceed 15%. Within this zone of high fault intensity, the rock is too highly deformed to permit the necessary measurements for strain calculations. However, in the relatively high intensity zone further from the fault, the rock has retained very good macroscopic integrity even with 8% to 15% $\bar{\varepsilon}$.

*Stress, strain and rotation*

The determination of the fault-strain tensor provides, of course, not only the equivalent strain but also the principal strain orientations and magnitudes (Table 2). In the following, $\varepsilon_1$ and $\varepsilon_3$ are the principal contractional and extensional strains, respectively, and a positive sign indicates extension. The finite-strain formulation is used in all cases. The skew-symmetric portion of the displacement-gradient tensor indicates the rotation, $\omega$, due to the fault displacements (see equation 6). The principal stress axes are inferred from the fault orientations.

The mesoscale faults in the Wingate form in mutually offsetting, quasi-conjugate (orthorhombic) systems with opposing offsets (Jamison & Stearns 1982). At some locations in the East Kodel's Canyon structure, the Wingate Sandstone appears to have rotated, relative to the stress field, during the course of deformation (Jamison & Stearns 1982). This is suggested by broad and overlapping distributions of the opposing-offset fault populations. However, the opposing-offset fault populations at all locations used in the current study are generally quite distinct (see Fig. 11), implying a very simple deformational history. The mutually offsetting relationship between conjugate populations indicates that the conjugate fault sets formed and slipped concurrently, and the existence of distinct populations of these conjugate fault sets suggests that the orientation of the stress field, relative to the rock, was effectively constant through the period of deformation.

For the purpose of inferring the stress orientations at the various sampling locations, the mean fault orientation for the faults with each offset direction is determined. These mean fault orientations are treated as conjugate faults, and the paleostress directions are inferred to be the bisectors of the intersection angles (e.g. Anderson 1942). The principal compressional stress ($\sigma_1$) is assumed to be the bisector of the acute intersection angle, and the principal tensional (or minimum compressional) stress ($\sigma_3$) the obtuse angle bisector. More rigorous approaches for the inference of paleostress orientation from fault data have been developed (e.g. Angelier 1979, Angelier *et al.* 1982). How-

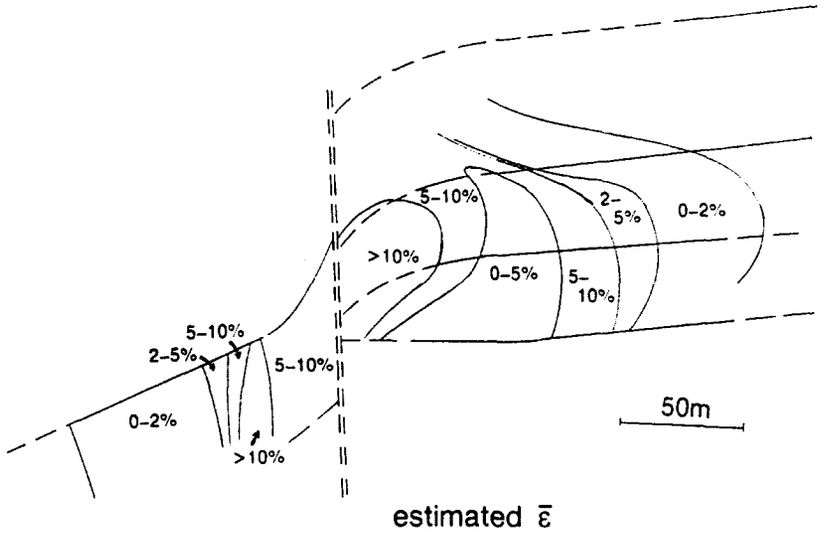


Fig. 10. Conversion of fault intensities (Fig. 7) into fault strains ($\bar{\varepsilon}$) using the piecewise-linear relationship shown in Fig. 9(b).

Table 2. Strain, stress and rotation at the measurement stations in East Kodel's Canyon (see Fig. 8 for station locations)

| Station | Phase of $\varepsilon_1$-axis | Phase of $\sigma_1$-axis | Dihedral angle (°) | $\sigma_1 \wedge \varepsilon_1$ (°) | $\omega$ (°) | $\bar{\varepsilon}$ (%) | Quality rating |
|---|---|---|---|---|---|---|---|
| A | 1.3°S | 18.4°N | 9.1 | 19.7 | 0.4 | 1.21 | M |
| B | 11.9°N | 16.6°N | 16.8 | 4.7 | 0.2 | 1.96 | A |
| C | 36.7°N | 19.1°N | 14.7 | 17.6 | −0.3 | 1.45 | A |
| D | 35.5°N | 16.3°N | 27.7 | −19.2 | −0.4 | 0.98 | A |
| E | 17.3°N | 18.1°N | 23.5 | 1.8 | 0.1 | 1.13 | M |
| F | 30.9°N | 11.9°N | 27.8 | −19.0 | −2.2 | 6.07 | M |
| G | 41.8°N | 18.1°N | 21.1 | −22.7 | −1.2 | 3.00 | M |
| H | 32.4°N | 11.0°N | 26.1 | −21.4 | −7.3 | 15.45 | M |
| I | 25.5°N | 6.0°N | 14.2 | −19.5 | −2.9 | 8.71 | M |
| J | 47.1°N | 18.4°N | 26.1 | −28.7 | −4.7 | 9.67 | A |
| K | 36.0°N | 17.3°N | 22.2 | −18.7 | −4.9 | 11.02 | M |
| L | 24.4°N | 12.3°N | 21.4 | −12.1 | −2.4 | 9.25 | M |
| M | 29.1°N | 4.5°N | 6.2 | −24.6 | −2.6 | 5.70 | S |
| N | 19.9°N | 8.3°N | 22.7 | −11.6 | −0.5 | 1.65 | A |
| O | 34.1°N | 17.9°N | 31.2 | −16.2 | −0.9 | 3.11 | A |
| P | 34.9°N | 23.9°N | 25.4 | −11.0 | −0.3 | 1.57 | M |
| Q | 37.5°N | 17.7°N | 24.6 | −19.8 | −1.6 | 3.05 | A |
| R | 41.0°N | 9.6°N | 16.6 | −31.4 | −4.5 | 9.48 | A |
| S | 46.0°N | 22.4°N | 22.2 | −23.6 | −2.5 | 6.15 | A |
| T | 48.5°N | 20.5°N | 15.5 | −28.0 | −5.1 | 10.68 | A |
| U | 7.6°S | 31.8°N | 8.8 | 24.2 | 6.1 | 12.17 | S |
| V | 54.0°N | 42.0°N | 7.0 | −12.0 | 5.4 | 9.99 | S |
| Average | | | 19.6 | 18.5 | | | |

ever, for conjugate faults in a constant stress field orientation, as is inferred to be the case developed here, the more sophisticated approaches should not provide significantly different results (Angelier 1979). The acute angle between the conjugate fault set in the Wingate is consistently quite small, averaging about 20° (Table 2).

The inferred $\sigma_1$-axes are generally at high angles to bedding, rotating slightly at locations close to the main fault (Fig. 12a). In previous work on this structure (Jamison & Stearns 1982), it was found that this rotation of the inferred $\sigma_1$-axis continues into the downthrown block, becoming almost horizontal at the northern limits of the faulting. The overall $\sigma_1$-axis pattern through East Kodel's Canyon actually matches the Hafner (1951) elastic analysis of simple block faulting quite well.

The $\varepsilon_1$-axes are more oblique to bedding than the $\sigma_1$-axes, but, in general, they do display a similar rotation towards the main fault (Fig. 12b). The calculated $\varepsilon_1$-axis and the inferred $\sigma_1$-axis at any given measurement station are distinctly non-coaxial. The angle between $\sigma_1$ and $\varepsilon_1$ ($\sigma_1 \wedge \varepsilon_1$) ranges from 2° to 31°, averaging 18.5°. This non-coaxiality is not simply a reflection of the rotation, $\omega$, for $\omega$ is generally much smaller than $\sigma_1 \wedge \varepsilon_1$. Also, $\omega$ exhibits a roughly linear relationship with $\bar{\varepsilon}$, whereas $\sigma_1 \wedge \varepsilon_1$ does not (Fig. 13). The non-coaxiality can be just as great in the incipient phases of faulting (low $\bar{\varepsilon}$) as in the advance stages of fault deformation.

Although $\omega$ and $\sigma_1 \wedge \varepsilon_1$ are not directly related, they both result from the same cause, viz., the unequal development of the conjugate fault systems. At most sampling locations in this study, one set of the fault conjugates is substantially better developed than the other, in terms both of number of faults and their cumulative offset. For example, at station I, 33 of the 50 faults are downdropping towards the main fault (i.e. down to the north). The sum of displacements on this N-dropping set of faults is 20.6 cm, as opposed to 9.3 cm on the conjugate system.

The specific effect that this unequal development of conjugate faults has on both $\omega$ and $\sigma_1 \wedge \varepsilon_1$ may be illustrated by first considering a single system of parallel faults (Fig. 14a). For small displacements (infinitesimal strains), $\varepsilon_1$ is at 45° to the fault surfaces. As displacements on these faults increase, the $\varepsilon_1$ angle, $\bar{\varepsilon}$, and $\omega$ all increase (Fig. 14b). Because there are no conjugates in this fault system, the principal stress axes cannot be determined (unless it is simply assumed to be at a specified angle to the fault surfaces). However, if a few conjugate faults are added to the original set of faults (Fig. 14c), the $\sigma_1$-axis may now be inferred. In this illustration, $\sigma_1 \wedge \varepsilon_1$ is 19°, an order of magnitude greater than the rotation ($\omega = 1.7°$).

This non-uniform development of conjugate shears is not only a common characteristic of the small-scale faulting in the Wingate, it is also a feature that has been recorded, though seldom emphasized, in many other field studies. Moreover, it has long, but perhaps not widely, been recognized that the potential for non-coaxiality between the principal stress and strain axes (resulting from the non-uniform development of the conjugate slip systems) is a general property of a Coulomb material (e.g. de Josselin de Jong 1958). In this example (Fig. 14), the conjugate systems intersect at an angle of 40°. This is less than the 60° intersection angle often cited for a Coulomb material, but still equal to or larger than the intersection angles observed in the Wingate and, indeed, in several other field and experimental studies (e.g. Muehlberger 1961, Aydin & Reches

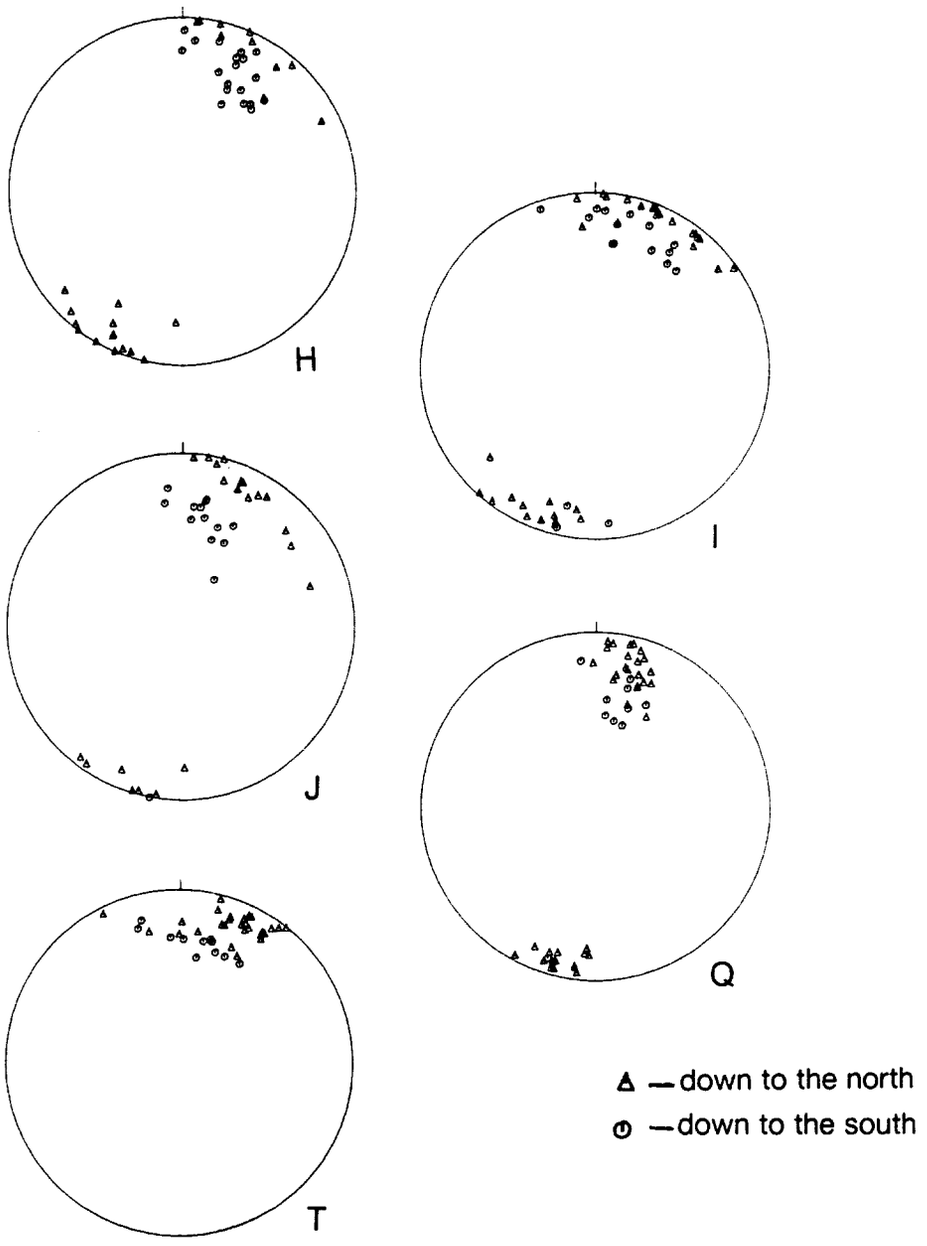


Fig. 11. Equal-area stereonet plots of poles to fault surfaces at several measurement stations on the East Kodel's Canyon structure (cf. Fig. 8).

1982, Underhill & Woodcock 1987). This observation has significance because the smaller the intersection angle between the conjugate systems, the larger the potential angular difference between $\sigma_1$ and $\varepsilon_1$ (de Josselin de Jong 1958).

The unequal development of the conjugate fault systems may be, in fact, an intrinsic property of a Coulomb material. This assertion derives from consideration of the deformational efficiency of the fault development. Note that $\bar{\varepsilon}$ has actually decreased with the addition of the conjugate faults to the initial system of parallel faults (see Fig. 14). The reason is simply that the displacement on the conjugate faults has negated some of the vertical offset produced by the initial set of faults (Fig. 15). The conjugates do add to the total horizontal offset, but, in this case, the loss in $dv$ is greater than the gain in $du$, and thus the overall drop in $\bar{\varepsilon}$. As long as the conjugate faults intersect at less than 90° (in which case the material becomes von Mises), their offsets will be at least partially negating. This will not necessarily result in a decrease in $\bar{\varepsilon}$ with the development of conjugate faults. However, it will be true that the greatest $\bar{\varepsilon}$ for a given cumulative fault displacement is produced by a single system of faults rather than conjugate sets.

## CONCLUSIONS

The deformation produced by faults, fractures and other discontinuous deformational features may be represented by a strain tensor. This representation is inherently imprecise because it equates a discontinuous phenomenon with a continuum measurement. Nonetheless, the strain representation does allow fault- and

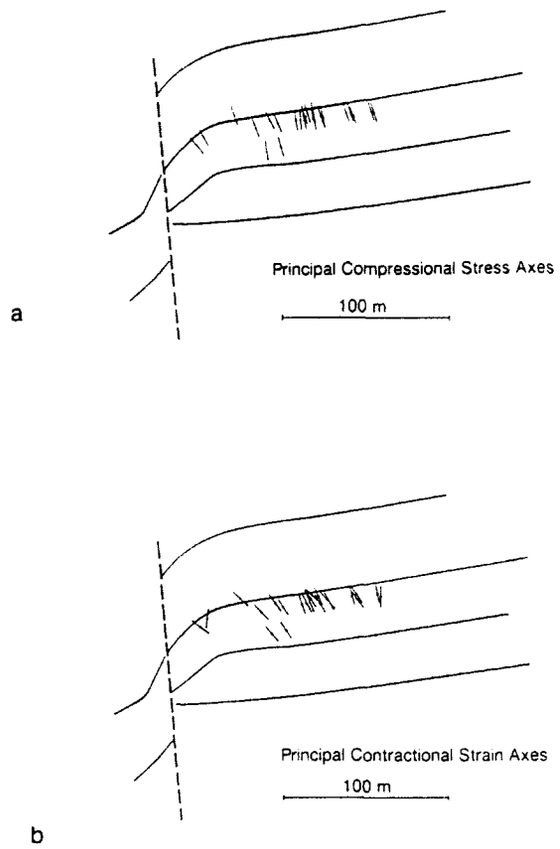


Fig. 12. Principal contractional strain and compressional stress axes at the East Kodel's Canyon measurement locations. (a) Inferred $\sigma_1$-axes. (b) Calculated $\varepsilon_1$-axes.

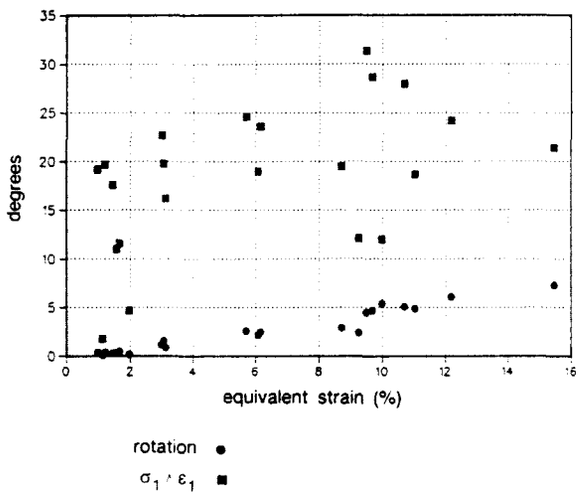


Fig. 13. The angle between the principal stress and principal strain axes ($\sigma_1 \wedge \varepsilon_1$) and the angle of rotation ($\omega$) at the East Kodel's Canyon measurement stations plotted as a function of equivalent strain ($\bar{\varepsilon}$).

fracture-associated deformation to be compared and related directly and quantitatively to other, relatively more continuous geologic deformation.

The maximum contractional fault strains ($\varepsilon_1$) measured in this study of the Wingate Sandstone range from −0.9% to −13.4%. Calculated strains derived from twinned calcite generally fall in this same range of $\varepsilon_1$ values (e.g. Groshong 1975, Spang *et al.* 1981, Groshong *et al.* 1984, Wiltschko *et al.* 1985). Various

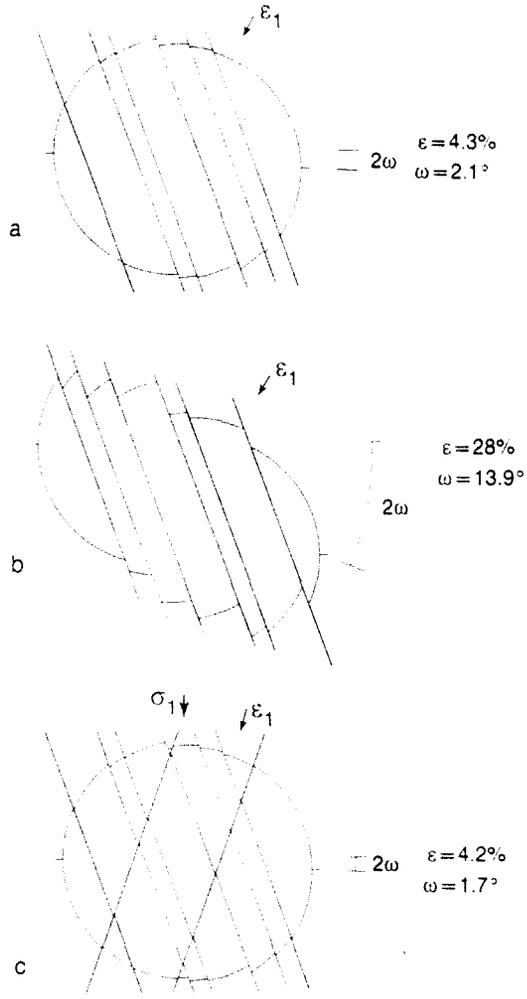


Fig. 14. Illustration of the specific effects of fault development on $\sigma_1$ and $\varepsilon_1$ orientations and $\omega$. (a) Parallel, small displacement faults produce simple shear. (b) Increasing displacement on these faults increases $\omega$, $\bar{\varepsilon}$, and the angle between the faults and the $\varepsilon_1$-axis. (c) The addition of conjugate faults allows the $\sigma_1$-axis to be inferred.

pressure-solution phenomena can also produce comparable amounts of shortening (e.g. Engelder 1979), but pressure solution can also produce considerably larger strains (e.g. Mosher 1980). The strain due to faulting can

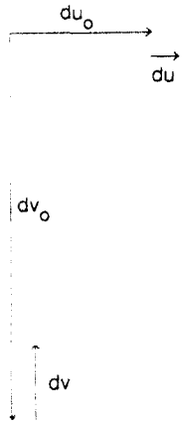


Fig. 15. Displacements in the horizontal and vertical directions due to the faults of Fig. 14(a) ($du_o$ and $dv_o$) and due to the added conjugate faults in Fig. 14(c) ($du$ and $dv$). Although cumulative fault displacement increases, the resultant strain, in this case, decreases.

certainly be greater than the values I have recorded. However, the practical limitations of obtaining the needed measurements in a highly faulted rock mass may prohibit the assessment of substantially larger fault strains.

The strain due to mesoscale faults can, thus, equal or exceed the strain that results from other deformation mechanisms common in unmetamorphosed terranes. The effects of these various strain-producing mechanisms are basically additive. Proper quantitative evaluation of tectonic deformation can be made only by assessing the effects of all the active mechanisms.

Expressing fault-associated deformation in terms of strain and rotation tensors also provides a clearer perception of the deformational characteristics of a Coulomb material. Most of our concepts regarding the deformation of a Coulomb material derive from rock mechanics experiments. In such experiments, the principal stress and strain axes are generally forced (or assumed) to be coaxial. In the Wingate Sandstone, the calculated strain and inferred stress axes are distinctly non-coaxial, even at very low strain values. These field observations suggest that a proper rheological characterization of Coulomb materials should at least allow, and perhaps require, such non-coaxiality, as has been suggested, for example, by de Josselin de Jong (1964) and Mandl & Fernández Luque (1970).

*Acknowledgements*—Special thanks to my colleague, Nigel Higgs, who has been very instrumental in developing the fault strain concept and also assisted in the data acquisition. This manuscript has benefitted from the critical reviews and comments of Bob Krantz, Martha Withjack, Nigel Higgs and an anonymous referee. I would like to thank Amoco Production Company for permission to publish this study, which was presented in a 1985 Amoco Research Report.

## REFERENCES

Anderson, E. M. 1942. *The Dynamics of Faulting*. Oliver and Boyd, Edinburgh.

Angelier, J. 1979. Determination of the near principal directions of stresses for a given fault population. *Tectonophysics* **56**, T17–T26.

Angelier, J., Tarantola, A., Valette, B. & Manoussis, S. 1982. Inversion of field data in fault tectonics to obtain the regional stress—I. Single phase fault populations. A new method of computing the stress tensor. *Geophys. J. R. astr. Soc.* **69**, 607–621.

Arthaud, F. 1969. Méthode de détermination graphique des directions de raccourcissement, d'allongement et intermédiaire d'une population de failles. *Bull. Soc. geol. Fr.* **11**, 729–737.

Aydin, A. & Johnson, A. M. 1978. Development of faults as zones of deformation bands and as slip surfaces in sandstone. *Pure & Appl. Geophys.* **116**, 931–942.

Aydin, A. & Reches, Z. 1982. Number and orientation of fault sets in the field and in experiments. *Geology* **10**, 107–112.

Bisplinghoff, R. L., Mar, J. W. & Pian, T. H. H. 1965. *Statics of Deformable Solids*. Addison-Wesley, Reading, Massachusetts.

de Josselin de Jong, G. 1958. The undefiniteness in kinematics for frictional materials. *Proc. Conf. Earth Pressure Problems, Brussels* **1**, 55–70.

de Josselin de Jong, G. 1964. Lower bound collapse theorem and lack of normality of strain rate to yield surface for soils. In: *Rheology and Soil Mechanics Symposium, Grenoble*. Springer, Berlin, 69–78.

Engelder, T. 1979. Mechanisms for strain within the Upper Devonian clastic sequence of the Appalachian Plateau, western New York. *Am. J. Sci.* **279**, 527–542.

Fung, Y. C. 1965. *Foundation of Solid Mechanics*. Prentice-Hall, Englewood Cliffs, New Jersey.

Gauthier, B. & Angelier, J. 1985. Fault tectonics and deformation: a method of quantification using field data. *Earth Planet. Sci. Lett.* **74**, 137–148.

Groshong, R. H., Jr. 1975. Strain, fractures, and pressure solution in natural single layer folds. *Bull. geol. Soc. Am.* **86**, 1363–1376.

Groshong, R. H., Jr., Pfiffner, O. A. & Pringle, L. R. 1984. Strain partitioning in the Helvetic thrust belt of eastern Switzerland from the leading edge to the internal zone. *J. Struct. Geol.* **6**, 5–18.

Hafner, W. 1951. Stress distribution and faulting. *Bull. geol. Soc. Am.* **80**, 2539–2550.

Jaeger, J. C. & Cook, N. G. 1969. *Fundamentals of Rock Mechanics*. Methuen, London.

Jamison, W. R. & Stearns, D. W. 1982. Tectonic deformation of Wingate Sandstone, Colorado National Monument. *Bull. Am. Ass. Petrol. Geol.* **66**, 2584–2608.

Krantz, R. W. 1988. Multiple fault sets and three-dimensional strain: theory and application. *J. Struct. Geol.* **10**, 225–237.

Lohman, S. W. 1965. Geology and artesian water supply of the Grand Junction area, Colorado. *Prof. Pap. U.S. geol. Surv.* **451**.

Mandl, G. & Fernández Luque, R. 1970. Fully developed plastic shear flow of granular materials. *Géotechnique* **20**, 277–307.

Mosher, S. 1980. Pressure solution deformation of conglomerates in shear zones, Narragansett Basin, Rhode Island. *J. Struct. Geol.* **3**, 219–224.

Muehlberger, W. R. 1961. Conjugate joint sets of small dihedral angle. *J. Geol.* **69**, 211–219.

Nye, J. F. 1972. *Physical Properties of Crystals: Their Representation by Tensors and Matrices*. Oxford University Press, London.

Reches, Z. 1978. Analysis of faulting in a three-dimensional strain field. *Tectonophysics* **47**, 109–129.

Spang, J. H., Wolcott, T. L. & Serra, S. 1981. Strain in the ramp regions of two minor thrusts, Southern Canadian Rocky Mountains. *Am. Geophys. Un. Geophys. Monogr.* **24**, 243–250.

Underhill, J. R. & Woodcook, N. H. 1987. Faulting mechanisms in high-porosity sandstones: New Red Sandstone, Arran, Scotland. *Spec. Publs geol. Soc. Lond.* **29**, 91–105.

Wiltschko, D. V., Medwedeff, D. A. & Millson, H. E. 1985. Distribution and mechanisms of strain within rocks on the northwest ramp of Pine Mountain block, southern Appalachian foreland: a field test of theory. *Bull. geol. Soc. Am.* **96**, 426–435.

## APPENDIX

*Finite and infinitesimal strain*

Finite strain in a Lagrangian description (referenced to the undeformed configuration) is represented by the Green strain tensor $\varepsilon_{ij}$ (e.g. Fung 1965) where, for two dimensions:

$$\varepsilon_{xx} = \frac{\partial u}{\partial x} + \frac{1}{2}\left\{\left(\frac{\partial u}{\partial x}\right)^2 + \left(\frac{\partial v}{\partial x}\right)^2\right\} \tag{A1}$$

$$\varepsilon_{yy} = \frac{\partial v}{\partial y} + \frac{1}{2}\left\{\left(\frac{\partial u}{\partial y}\right)^2 + \left(\frac{\partial v}{\partial y}\right)^2\right\} \tag{A2}$$

$$\varepsilon_{xy} = \varepsilon_{yx} = \frac{1}{2}\left\{\frac{\partial v}{\partial x} + \frac{\partial u}{\partial y} + \frac{\partial u}{\partial x}\frac{\partial u}{\partial y} + \frac{\partial v}{\partial x}\frac{\partial v}{\partial y}\right\}. \tag{A3}$$

For very small (infinitesimal) strains, the second-order terms are insignificant and are dropped. Consequently, the strain tensor is equal to the symmetric portion of the displacement-gradient tensor, $D_{ij}$ (see text). However, the finite strains may also be expressed in terms of the components of $D_{ij}$ (see equation 1) as

$$\varepsilon_{ij} = \tfrac{1}{2}\{D_{ij} + D_{ji} + D_{1i}D_{1j} + D_{2i}D_{2j}\}. \tag{A4}$$

*Strain for non-shear discontinuities*

Extension fractures (joints) and stylolites also produce discontinuous deformation. A strain representation for these features may be derived in a fashion parallel to the fault-strain tensor. For the extensional features (Fig. A1a), the initial displacement-gradient tensor is approximated by

$$D_{ij} = \begin{bmatrix} e/d & 0 \\ 0 & 0 \end{bmatrix}. \tag{A5}$$

Rotation to a reference co-ordinate system produces

$$D_{mn} = \frac{e}{d}\begin{bmatrix} \sin^2\theta & \sin\theta\cos\theta \\ \sin\theta\cos\theta & \cos^2\theta \end{bmatrix}. \tag{A6}$$

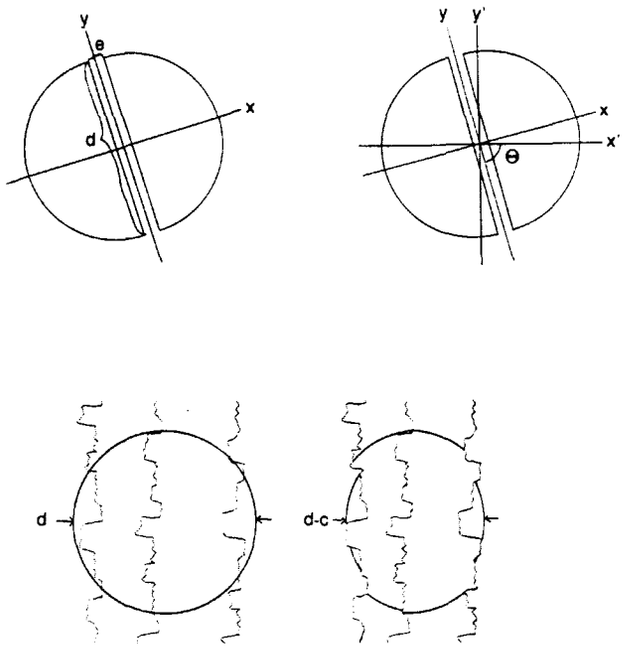


Fig. A1. Determination of the displacement-gradient tensor, in two dimensions, for extensional and contractional discontinuities. (a) Extension $e$ across a discontinuity (e.g. joint) parallel to the $y$-axis. (b) Contraction $c$ across a discontinuity (e.g. stylolite) parallel to the $y$-axis.

For the contractional features (Fig. A1b), $e$ is replaced by $-c$ in the displacement-gradient tensor. Note that the displacement-gradient tensor for these non-shear discontinuities is symmetric. There is no skew-symmetric component. These features do not produce any rotation.

*Three-dimensional strain representation*

The development of a fault-strain tensor for three-dimensional deformation is, of course, analogous to the two-dimensional case. The existence of nine rather than four terms in the tensors simply makes book-keeping more laborious. For the case of a shear fracture or fault in the $xz$-plane (Fig. A2a), with displacement $s$ parallel to the $z$-axis, the only non-zero component of $D_{ij}$ is $D_{32}$; i.e. $dw/dy$. For a sphere of diameter $d$ in the undeformed state, the displacement-gradient tensor $(D_{ij})$ in this reference system is

$$D_{ij}^{\times} = \begin{bmatrix} 0 & 0 & 0 \\ 0 & 0 & 0 \\ 0 & s/d & 0 \end{bmatrix}. \tag{A7}$$

Transformation to a general reference system yields

$$D_{mn}^{\times} = \frac{s}{d} \begin{bmatrix} a_{13}a_{12} & a_{13}a_{22} & a_{13}a_{32} \\ a_{23}a_{12} & a_{23}a_{22} & a_{23}a_{32} \\ a_{33}a_{12} & a_{33}a_{22} & a_{33}a_{32} \end{bmatrix}. \tag{A8}$$

This tensor contains six direction cosines $(a_{ij})$ relating the general reference axes to the initial co-ordinates. These may be expressed in terms of four angles, viz., $\theta$, $\varphi$, $\delta$ and $\zeta$ (Fig. A2b):

$$a_{13} = \cos\delta\cos\zeta \tag{A9}$$

$$a_{23} = -\sin\zeta \tag{A10}$$

$$a_{33} = \cos\zeta\sin\delta \tag{A11}$$

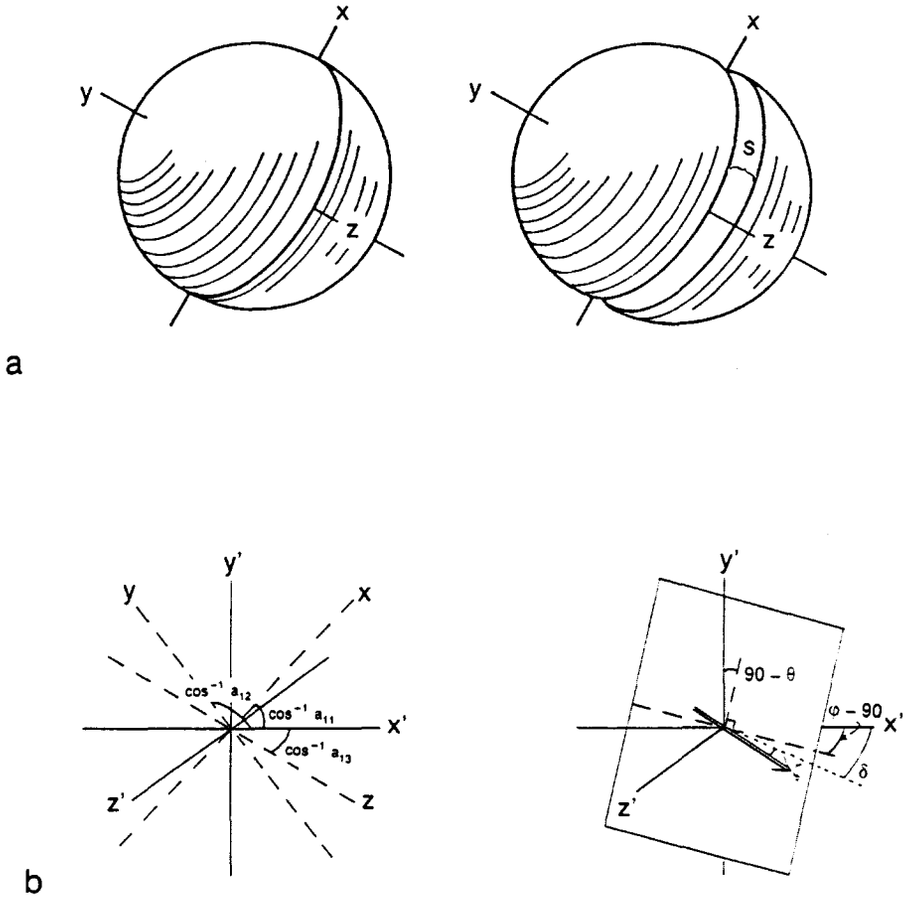


Fig. A2. Determination of the displacement-gradient tensor, in three dimensions, for faulting. (a) Displacement $s$ parallel to the $z$-axis along a fault parallel to the $x$–$z$-plane. (b) Rotation to reference co-ordinate system $x'y'z'$.

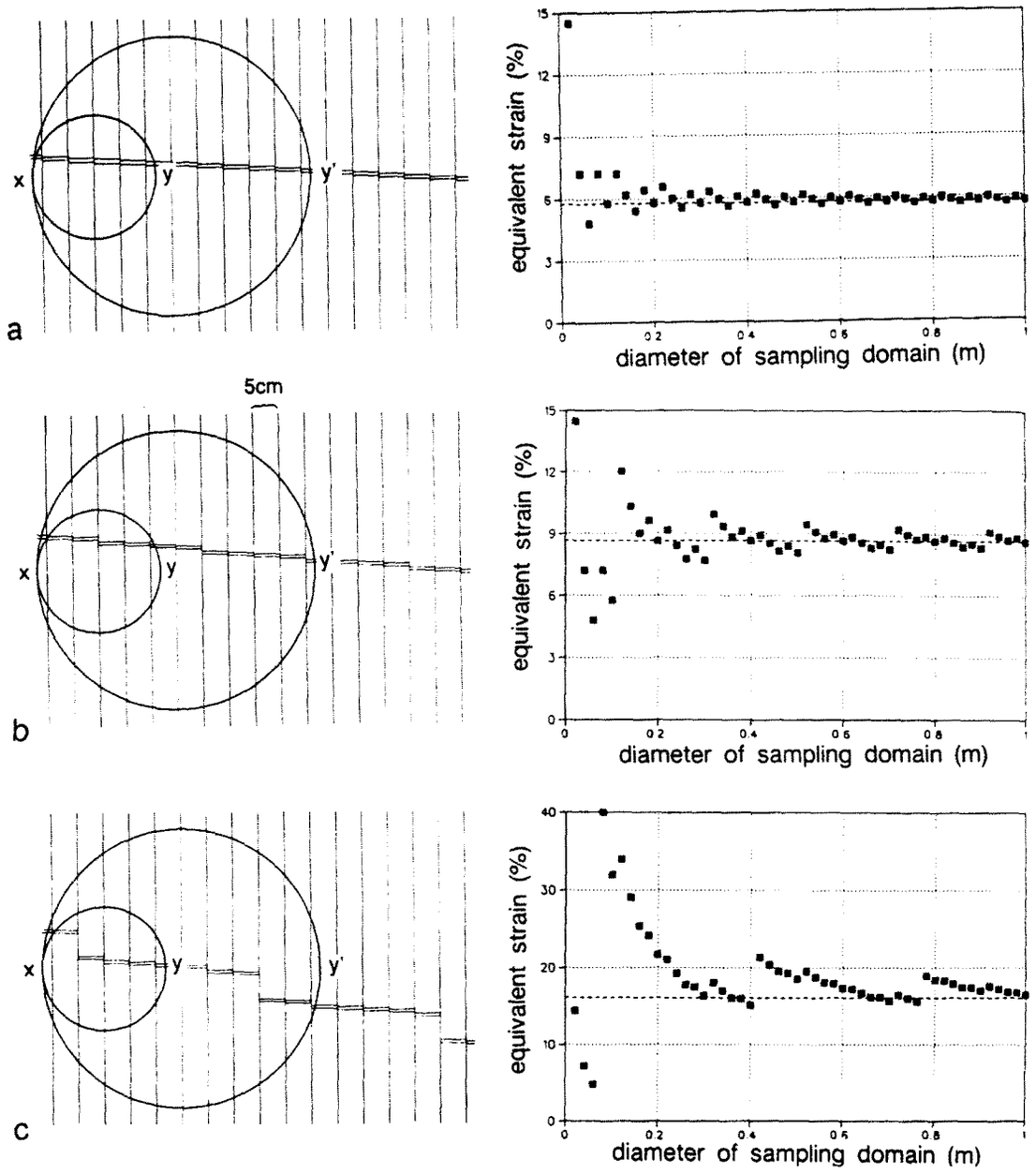


Fig. A3. Investigation of the effects of sampling domain size on the calculated $\bar{\varepsilon}$. (a) Uniformly spaced faults, each having 0.5 cm displacement. (b) Bimodal displacement fault population ($s$ = 0.5 and 1.5 cm). (c) Trimodal displacement fault population ($s$ = 0.5, 1.5 and 5.0 cm).

$$a_{12} = \cos\varphi \sin\theta \quad \text{(A12)}$$

$$a_{22} = \cos\theta \quad \text{(A13)}$$

$$a_{32} = \sin\varphi \sin\theta. \quad \text{(A14)}$$

If the general reference axes ($x'$, $y'$ and $z'$) are north, up and east, respectively, then $\theta$ is the dip of the fault surface, $\varphi$ is the dip direction, $\zeta$ is the plunge of the slip direction and $\delta$ is the bearing of the slip direction.

The finite strain, expressed in terms of the components of the displacement-gradient tensor, is

$$\varepsilon_{ij} = \tfrac{1}{2}\{D_{ij} + D_{ji} + D_{1i}D_{1j} + D_{2i}D_{2j} + D_{3i}D_{3j}\}. \quad \text{(A15)}$$

Again, second-order terms are insignificant at infinitesimal strains.

*Sampling domain size*

The effect that sampling domain size has on the calculated fault strain may be demonstrated by varying the domain size used in the sampling of some very uniform fault populations. Three hypothetical fault populations are considered. In each case, all faults in the population have the same orientation and sense of offset, and they are uniformly spaced 5 cm apart (Fig. A3). The sampling domain is a circle of diameter $XY_i$. Point X is fixed. The points $Y_i$ are spaced 2 cm apart along the horizontal line passing through point X. Choosing point $Y_1$ to be 2 cm from point X, and setting $i$ = 1, 50, a total of 50 sampling domains are available, with diameters ranging from 2 cm to 1 m, in 2 cm increments. The fault strain, $\bar{\varepsilon}$, is calculated at each of these increments. Plane (two-dimensional) strain is assumed.

In the simplest case (Fig. A3a), the faults all have the same displacement ($s$ = 0.5 cm). The fault strains ($\bar{\varepsilon}$) calculated for specific sampling domain diameters are indicated by the squares on the graphs (Fig. A3). The dashed horizontal line is the 'continuum' $\bar{\varepsilon}$. It is determined by letting the diameter of the sampling domain become very large ($XY_n \rightarrow \infty$).

The calculated $\bar{\varepsilon}$ can be significantly different from the continuum $\bar{\varepsilon}$ for sampling domains with diameters less than about 15 cm, or three times the fault spacing (Fig. A3a). For sampling domain diameters up to about 25 cm, or five times fault spacing, the calculated $\bar{\varepsilon}$ may differ from the continuum $\bar{\varepsilon}$ by as much as 10%. Even as the domain diameter becomes quite large (relative to fault spacing), a slight variance between calculated and continuum $\bar{\varepsilon}$ values persists. This discrepancy is never entirely eliminated, but it is minimized by a large sampling domain.

In the natural fault populations examined in the Wingate Sandstone, larger offset faults are commonly observed to be spaced further apart than smaller offset faults. In a second hypothetical population, every fourth fault (spacing = 20 cm) has an offset of 1.5 cm, while the remainder of the faults (spacing = 5 cm) have 0.5 cm offset (Fig. A3b). A marked increase in the calculated $\bar{\varepsilon}$ with increasing domain diameter occurs each time an additional large-offset fault is included in the sample population. Significant differences between calculated and continuum $\bar{\varepsilon}$ can occur at sampling domain diameters less than about 60 cm, or three times the spacing of the larger faults. Even with a larger sampling domain, a poor value of $\bar{\varepsilon}$ will result from barely including (or not including) one of the larger faults.

The third hypothetical fault population is even more complex. Every seventh fault (spacing = 35 cm) has 5.0 cm offset, every fourth (spacing = 20 cm) has 1.5 cm displacement, and the rest are each offset 0.5 cm (Fig. A3c). Once again, a substantial increase in the calculated $\bar{\varepsilon}$ occurs each time an additional large-offset fault is incorporated into the sampling domain. The addition of each intermediate-displacement fault is also detectable, though the effect is overshadowed by the imprint of the larger faults. I would suggest that the deviation between calculated $\bar{\varepsilon}$ and the continuum $\bar{\varepsilon}$ is becoming 'acceptably' small when at least three of the largest displacement faults are included in the sample.

In summary, a sampling domain large enough to include at least three of the largest-offset faults appears to be needed to ensure against poor $\bar{\varepsilon}$ calculation. This is, of course, a subjective evaluation. It also appears to be important to choose end points for the sample domain diameter that are not too close to the larger-displacement faults.